RESEARCH PAPER

Seismic Behavior of Bolted Endplate Connection Between Steel Reinforced Concrete (SRC) Wall and SRC Beam for Use in High-Rise Buildings

Yuntian Wu[1] · Daoyang Kang[1] · Long Gao[1] · Yiting Su[1] · Yeongbin Yang[1]

Abstract

To improve the constructability of the steel and concrete composite coupled wall system while maintaining good seismic performance in terms of strength, stiffness and energy dissipation capacity, the bolted endplate connection between steel reinforced concrete (SRC) wall and SRC beam has been proposed and studied. The endplate is shop welded to the end of steel beam and then fastened to the flange of steel column at boundary element of wall pier through high-strength bolts before the fabrication of reinforcement cage and concrete pouring for the composite beams. Five SRC beam-SRC wall subassembly specimens were designed, constructed and tested subjected to cyclic displacement reversals at SRC beam end. The test parameters included the amount of steel plate embedded in SRC beams and the influence of slab. The responses of the specimens in terms of load–displacement hysteretic responses, cracking patterns, ductility, strength and stiffness degradation characteristics were discussed. The test results show that through rational design the bolted endplate connection can satisfactorily ensure the load transfer mechanism between SRC beam and SRC wall such that the SRC beam can fully develop its strength, ductility, post-yield strength and stiffness retention capacities. The strength, post-yield deformation and energy dissipation capacity of SRC coupling beams can be effectively enhanced by increasing the steel plate ratio. The existence of slab can enhance the overall seismic performance of SRC beam. Nonlinear finite element modeling approach was developed and verified by comparison with the test results, showing good agreement in terms of the skeleton and hysteresis curves.

Keywords Endplate · Connection · Coupled wall · Composite structure · Seismic behavior · Finite element analysis

List of symbols

V_{steel}	The shear capacity of steel plate
V_{RC}	The shear capacity of concrete encasement
V_u	The theoretical ultimate shear capacity
θ	The beam rotation
L	The clear beam span length
V_{max}	The maximum measured shear
V_m	The maximum shear force
Δ	Vertical displacement at the top of the shear wall
Δ_u	The maximum displacement
Δ_y	The yield displacement
μ_Δ	The displacement ductility coefficient
$\varepsilon_{c/3}$	The strain at which one-third of the maximum compressive strength is reached
ε_c	The strain at which the maximum compressive strength is reached
ε_u	The ultimate strain at which the material is completely softened in compression
f_c	Compressive strength of concrete
f_t	Tensile strength of concrete
E	Young's modulus
G_c	The total compressive fracture energy
G_F	The total tensile fracture energy
h	The characteristic element length
τ_{max}	The bond strength
τ_f	The residual bond stress

✉ Yuntian Wu
   yuntianw@cqu.edu.cn

   Daoyang Kang
   dykang@cqu.edu.cn

   Long Gao
   longgao@cqu.edu.cn

   Yiting Su
   ytSu@cqu.edu.cn

   Yeongbin Yang
   ybyang@cqu.edu.cn

[1] School of civil engineering, Chongqing University, 83, Shabei Street, Shapingba District, Chongqing, China

s The relative slip between steel and concrete
β The empirical coefficient

1 Introduction

As an efficient structural system to resist lateral forces, the reinforced concrete (RC) coupled shear wall has been widely used for substantial lateral load-carrying capacity, stiffness and energy dissipation capacity. For super high-rise buildings, however, RC walls may not be adequate at the bottom story, where the shear wall is subjected to high levels of axial load, flexural moment and shear during strong earthquake excitations. By introducing steel shapes, the axial load-carrying capacity and lateral force resisting mechanism of RC walls can be significantly improved without much increase in wall thickness, resulting in the so-called steel reinforced concrete (SRC) composite walls. The most fundamental type of SRC composite walls frequently used in super high-rise buildings contains embedded H-shaped steel columns at the boundary elements. To achieve even better seismic performance, steel plate or diagonal braces can be added at web of wall between the H-shaped steel columns at boundary elements, as shown in Fig. 1. Previous research [1–4] has demonstrated that SRC composite shear walls can be designed to have excellent seismic performance in terms of load-carrying capacity, post-yield deformation and energy dissipation capacities.

Similar trend can also be seen in the development of coupling beams in RC coupled shear walls. To improve the ductility and energy dissipation capacity under large shear deformation reversals, SRC composite coupling beams where steel plate is embedded in RC coupling beam has been proposed and studied by Lam et al. [5], Gong and Shahrooz [6, 7] and Nie [8]. Research results indicated that the key to the successful application of SRC beams is the selection of embedment length of steel plate into RC wall piers. With adequate embedment length and appropriate detailing, steel and concrete composite coupling beams can exhibit excellent seismic behavior in terms of post-yield deformation, ductility and energy dissipation.

However, direct embedment connection details cannot be applied to join SRC beams and SRC wall piers due to the existence of embedded H-shaped steel column at boundary elements of wall piers. A conventional solution to this
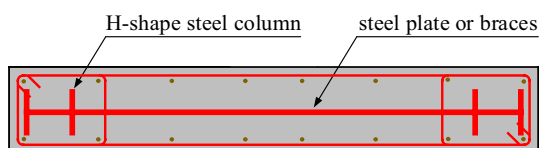
problem is to field weld the steel shapes of composite coupling beams to the flanges of embedded steel shapes at boundary elements of the composite wall piers. It is without doubt, however, that the field welding may cause difficulties in construction and quality control, resulting in the increase of overall construction cost. To achieve better constructability, it is necessary to develop an alternative type of connection for composite coupling beams and composite wall piers that is not only convenient for construction but also adequate to ensure the performance objectives of composite coupling beams.

To provide connection details with good constructability for SRC beam and SRC wall, the bolted endplate connection was introduced to join SRC beams and SRC composite wall piers, as shown in Fig. 2. The endplate is shop welded to the end of steel beam and then fastened to the flange of steel column at boundary element of wall pier through high-strength bolts before the fabrication of reinforcement cage and concrete pouring for the composite beams. It is obvious that the bolted endplate connection can eliminate filed welding and only bolting is required on the construction site. Although a few relevant research has been done (e.g., Li [9], Wu [10], Prinz [11], Mohamadi-Shooreh [12], Asghari [13], Choi [14], Hung [15], Qun [16] and Wang [17]), research on bolted endplate connections for joining coupling beam and wall pier has rarely been conducted. In this research project, experimental program was carried out to examine the load transfer mechanism between SRC beams and SRC wall piers. The damage development process, strength and stiffness degradation characteristics, and failure patterns were investigated through the interpretation of test results. Numerical study was further conducted to develop appropriate modeling techniques. And numerical analysis results were compared with those obtained from tests to verify the effectiveness and accuracy of the numerical approach.
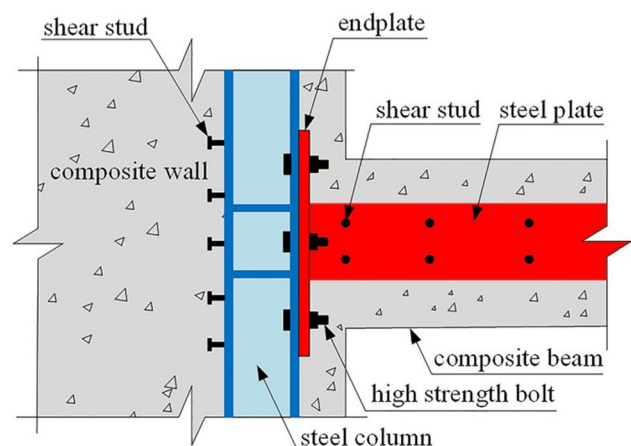
Fig. 2 Bolted endplate connection for composite beam and composite wall pier

Fig. 1 Typical steel–concrete composite wall detail

1.1 Experimental Program

The emphasis of the experimental program was placed on the adequacy of proposed bolted endplate connection for the transfer of flexural moment and shear from SRC beams to SRC wall piers, accompanied by the full development of ductility and energy dissipation capacity of SRC beams. Therefore, each specimen was loaded at the beam end till the full capacities of beams were developed in terms of strength, post-yield deformation and energy dissipation. The corresponding responses of wall piers, especially the joint regions, were observed.

1.2 Details of Specimens

Five one-fourth-scale SRC beam-wall joint specimens identified by JS-1 to JS-5 were designed and constructed according to GB500010-2011 [18] and JGJ138-2012 [19]. Each specimen included a SRC wall pier and one-half of SRC beam. The wall piers of all specimens had the same geometry and dimensions, consisting of a 1000 mm×350 mm×300 mm loading block on top, a 1600 mm×400 mm×400 mm foundation at bottom and a 1200 mm×900 mm×220 mm wall portion in between, which was to be axially loaded during testing. The sizes of steel plate embedded in SRC beams varied. The steel plate ratios ρ_{sp}, defined as the ratio of cross sectional area of steel plate to that of the overall cross section of SRC beam, were 0.97% for specimens JS-1 and JS-2, 1.94% for specimens JS-3 and JS-4 and 4.36% for specimen JS-5, respectively. For specimens JS-2 and JS-4, overhanging flanges were included on top of the SRC beam section to consider the influence of slab. The dimensions of endplate were selected based on the yield line theory, ignoring the favorable influence of the surrounding concrete and reinforcement at boundary elements of wall piers [20].

Assuming that the total shear capacity of a SRC beam is the combination of the shear capacity of steel plate V_{steel} and that of concrete encasement V_{RC}, the SRC beams for specimens JS-1 to JS-4 were designed to have identical shear capacity by adjusting the contribution of the steel plate and the concrete encasement. Although the steel plate

ratio for beams of JS-3 and JS-4 was higher than that for beams of JS-1 and JS-2, the transverse reinforcement spacing was increased from 60 to 100 mm in JS-3 and JS-4 so as to reduce the shear capacity contributed by the concrete encasement for beams in JS-3 and JS-4. In addition, the influence of slab on the shear capacity of SRC beam was ignored. It is noted that the shear capacity contributed by the concrete encasement was calculated based on classical assumptions that can lead to underestimation. The bolted endplate connections of the specimens were designed based on the shear force demand of 1.6 ($V_{steel} + V_{RC}$) [7]. The parameters of specimens are summarized in Table 1 and the details of specimens are illustrated in Fig. 3.

1.3 Test Setup and Loading Regimen

Each of the specimens was subjected to constant axial loads on top of wall pier and vertical quasi-static load reversals at the free end of beam. The axial load representing an axial load ratio of 0.2 was applied by a hydraulic jack with 2000kN loading capacity and maintained approximately constant during testing. Lateral deformation of wall pier was not simulated for the current phase of study. The SRC coupling beams, as the first seismic resisting element, were designed to suffer most of the inelastic deformation and damage. By the mid-span inflection point assumption, the SRC beam representing one-half of the coupling beam span was subjected to cyclic reversed vertical loading by a servo-controlled hydraulic actuator with 1500 kN loading capacity and a stroke of 100 mm connected to the beam free end. The pushing down of SRC beam was designated as the positive loading direction while pulling up the negative direction. Two jacks were also placed against the front and rear surfaces of the foundation of specimens to avoid horizontal sliding. Rigid beams were used to compress the foundation to prevent the overturning of specimens through post-tensioning to the strong floor with high-strength steel rods. The test setup is illustrated in Fig. 4.

After the application of constant axial load to wall piers, the specimens were tested under reversed cyclic loading applied at the SRC beam end. The first cycles were load controlled, in

Table 1 Test matrix

ID	Embedded steel column (mm)	Steel plate (mm)	ρ_{sp} (%)	Endplate (mm)	Beam section (mm)	Transverse hoops in beam
JS-1	110×130×8×12	490×80×8	0.97	340×130×14	300×220	No.8@60
JS-2	110×130×8×12	490×80×8	0.97	340×130×14	300×940×220×60	No.8@60
JS-3	110×130×8×12	480×160×8	1.94	430×130×16	300×220	No.6@100
JS-4	110×130×8×12	480×160×8	1.94	430×130×16	300×940×220×60	No.6@100
JS-5	110×130×12×14	480×240×12	4.36	430×130×18	300×220	No.8@80

Fig. 3 Details of specimens
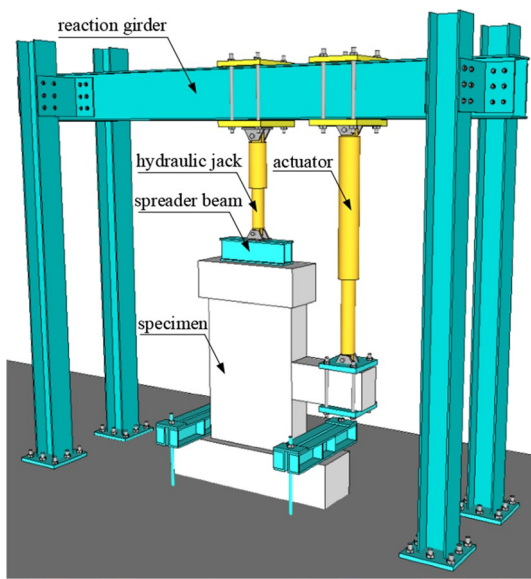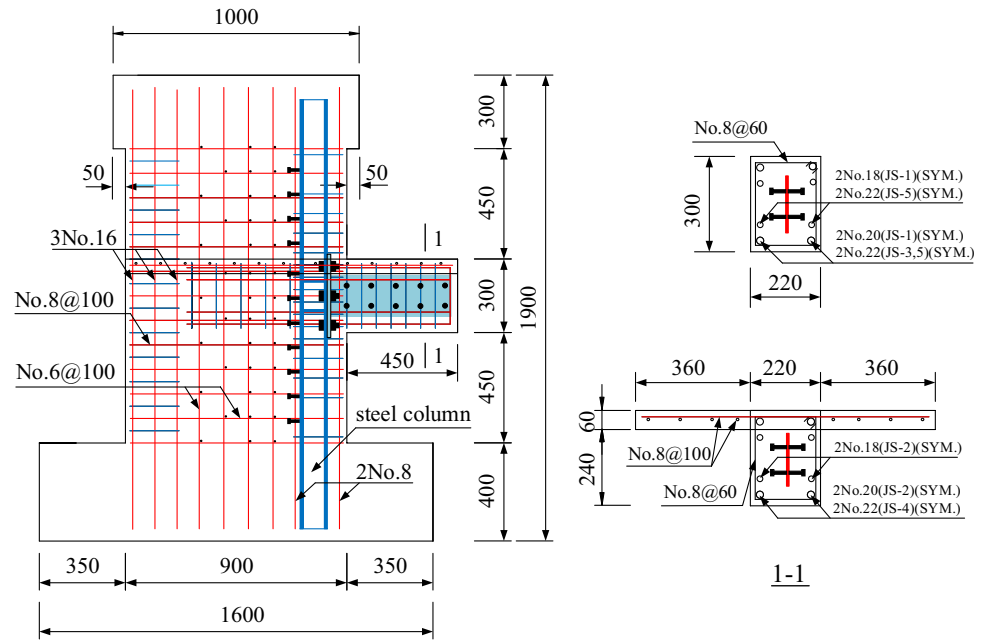
Fig. 4 Test setup

which each specimen was loaded to peak loads corresponding to 25, 50 and 75% of the theoretical ultimate shear capacity V_u. The subsequent cycles were displacement controlled, in which the specimen was displaced to unity ductility factor (μ) for two cycles, then to each successive ductility factors of 1.5, 2.0, 3.0, 4.0, etc., for two cycles. The beam rotation (θ) was defined as the differential displacement between the loading point at beam end and the beam-to-wall interface divided by the clear beam span length L. The average of values corresponding to the positive and negative peak loads at $0.75V_u$ in the first cycle was extrapolated by a factor of 4/3 to obtain the yield rotation

(θ_y) at $\mu = 1.0$. Each test was terminated when the peak load reached in the first cycle of a given ductility level dropped below 80% of the maximum measured shear (V_{max}).

1.4 Instrumentation

A series of measuring devices were utilized in tests to measure and record strain, deformation and load. Strain gages were attached to selected locations on reinforcing bars and steel shapes in SRC walls and beams to monitor the plasticity development process. Dial indicators were mounted on the surface of beam and beam-to-wall joint region to measure the deformation characteristics.

1.5 Material Properties

The concrete with specified compressive strength of 40 MPa was used for all specimens. The average compressive strengths of 150 mm × 150 mm × 150 mm cubic samples taken from the batches of concrete used for the five specimens and measured on the 28th curing day were 44.5, 43.1, 40.3, 38.3 and 39.7 MPa, respectively. The steel shapes used in all specimens were Q345B type with specified yield strength of 345 MPa. The main mechanical properties of reinforcing bars, steel shapes and steel plates are listed in Table 2.

2 Experimental Observations and Results

Based on the test parameters, influences of steel plate ratio of SRC beam and slab on the cracking and damage patterns of specimens were observed. The steel plate ratios of

Table 2 Mechanical properties of steel materials (MPa)

Material	f_y	f_t	E_s
Steel plate (8 mm thickness)	326.6	445.2	189,388
Steel plate (12 mm thickness)	342.4	494.5	184,241
Steel plate (14 mm thickness)	362.0	567.3	200,330
Steel plate (16 mm thickness)	363.4	551.5	176,379
No. 6 bars	392.1	493.0	2.07×105
No. 8 bars	416.8	516.7	2.10×105
No. 16 bars	432.5	606.7	1.98×105
No. 18 bars	451.5	632.4	2.01×105
No. 20 bars	472.6	594.6	1.94×105
No. 22 bars	463.1	572.8	2.05×105

specimens JS-1, JS-3 and JS-5 were 0.97, 1.94 and 4.36%, respectively. Specimens JS-2 and JS-4 had overhanging flanges for SRC beams, where steel plate ratios were the same as those of JS-1 and JS-3, respectively.

2.1 Cracking and Damage Patterns

The ultimate damage patterns of the five specimens are illustrated in Fig. 5. Flexural cracks first appeared at the top and bottom corners of beam–wall interface. Along with the increase of loading, inclined shear-flexural cracks were then developed on the beam side surfaces. And cracks at the top and bottom corners of beam–wall interfaces became through the entire beam width. During the further development of the inclined cracks on beam side surfaces, the beam-wall joint region also showed shear-flexural diagonal cracks. For specimen JS-1, when the vertical displacement at beam end was $2.0\Delta_y$, the maximum shear capacity of the SRC beam was reached. And more inclined cracks appeared on beam side surfaces and the cracks were widened. Then the peak shear capacity corresponding to subsequent loading cycles started to drop. The side surface concrete of beam web at mid-span cracked severely and spalled off. The test was terminated at loading cycles corresponding to peak vertical displacement of $3.0\Delta_y$. For specimens JS-3 and JS-5, the beam web concrete cracked and spalled off even more severely than JS-1 at ultimate condition, due to the fact that the beams of JS-3 and JS-5 could endure more shear reversals before failure. For specimens JS-2 and JS-4 with overhanging flanges, the cracking and spalling off of beam web concrete was less significant than JS-1 and JS-3, respectively, indicating the beneficial effect of slab on the damage mitigation of coupling beams. In addition, the cracking development was delayed in specimens with overhanging flanges as compared with those without overhanging flanges.

2.2 Load–Displacement Responses

Figure 6 shows the shear force versus vertical displacement hysteretic loops of the specimens. It can be easily seen that the existence of overhanging flanges increased the maximum
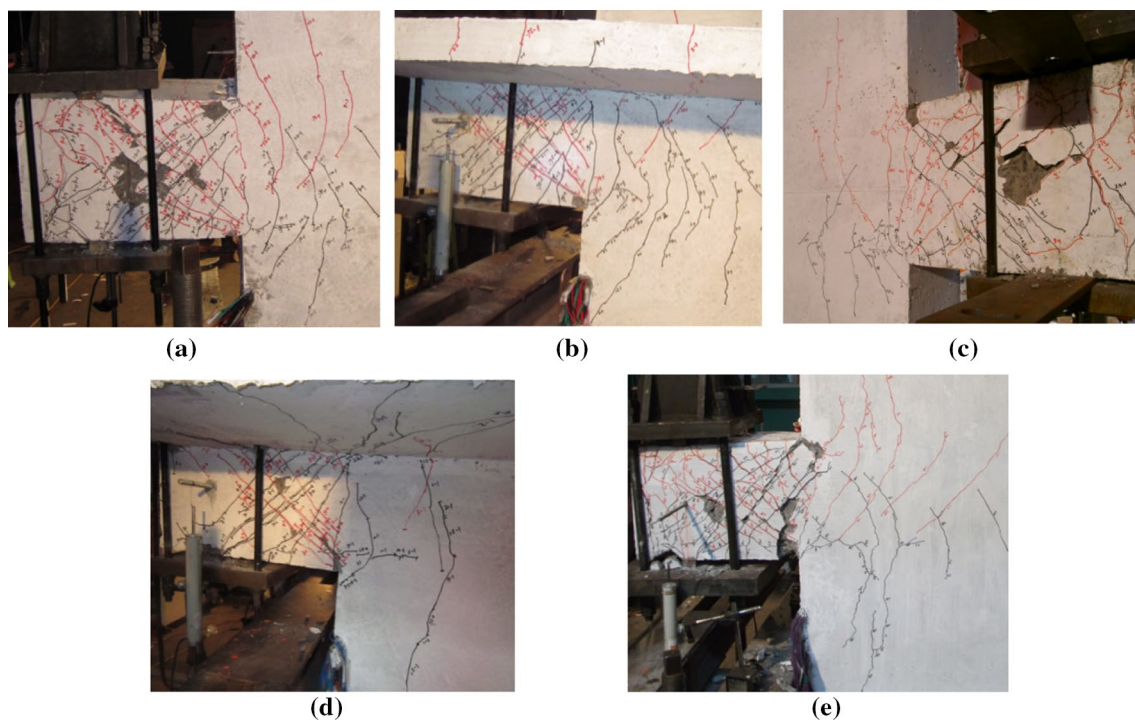
Fig. 5 Failure pattern of specimens: **a** JS-1; **b** JS-2; **c** JS-3; **d** JS-4; **e** JS-5

shear capacity and the strength capacity while had insignificant influence on the shape of hysteretic loops. The pinching effect of hysteresis loops of specimens JS-1 and JS-2 was more obvious than specimens JS-3 and JS-4. The hysteresis loops of specimen JS-5 exhibited the best energy dissipation characteristic with the least pinching effect, showing the increase of steel plate ratio of embedded steel plate can improve the energy dissipation capacity.

2.3 Strength and Ductility

From the load versus displacement skeleton curves of the specimens as shown in Fig. 7, it was apparent that specimen JS-5, which was provided with the largest steel plate ratio for the SRC beam, exhibited the highest stiffness and maximum shear capacity with rather gradual post-yield strength degradation. Specimens JS-2 and JS-4, in which slab influence was considered, also exhibited better strength and post-yield strength degradation characteristic than specimens JS-1 and JS-3 with rectangular beam cross sections. Although only the web was accounted for when calculating the nominal shear capacity of the SRC beam, the shear capacity of JS-2 was approximately 16% higher than that of JS-1, and the shear capacity of JS-4 was approximately 20% higher than JS-3, indicating that the existence of slab
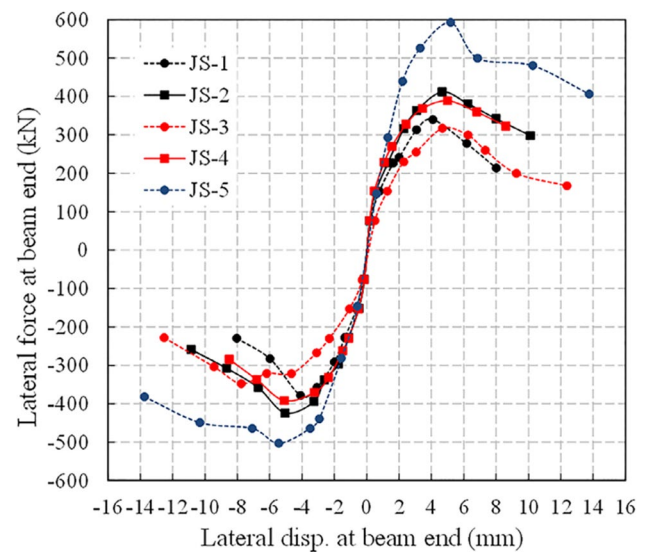
Fig. 7 Skeleton curves of specimens

can increase the strength of coupling beam. As discussed previously, the ultimate capacity of the SRC beams may be approximately 1.6 ($V_{steel} + V_{RC}$). For specimens JS-2 and JS-4, where slab was considered, the ratios of the measured to the nominal shear capacity were 1.60 and 1.65,
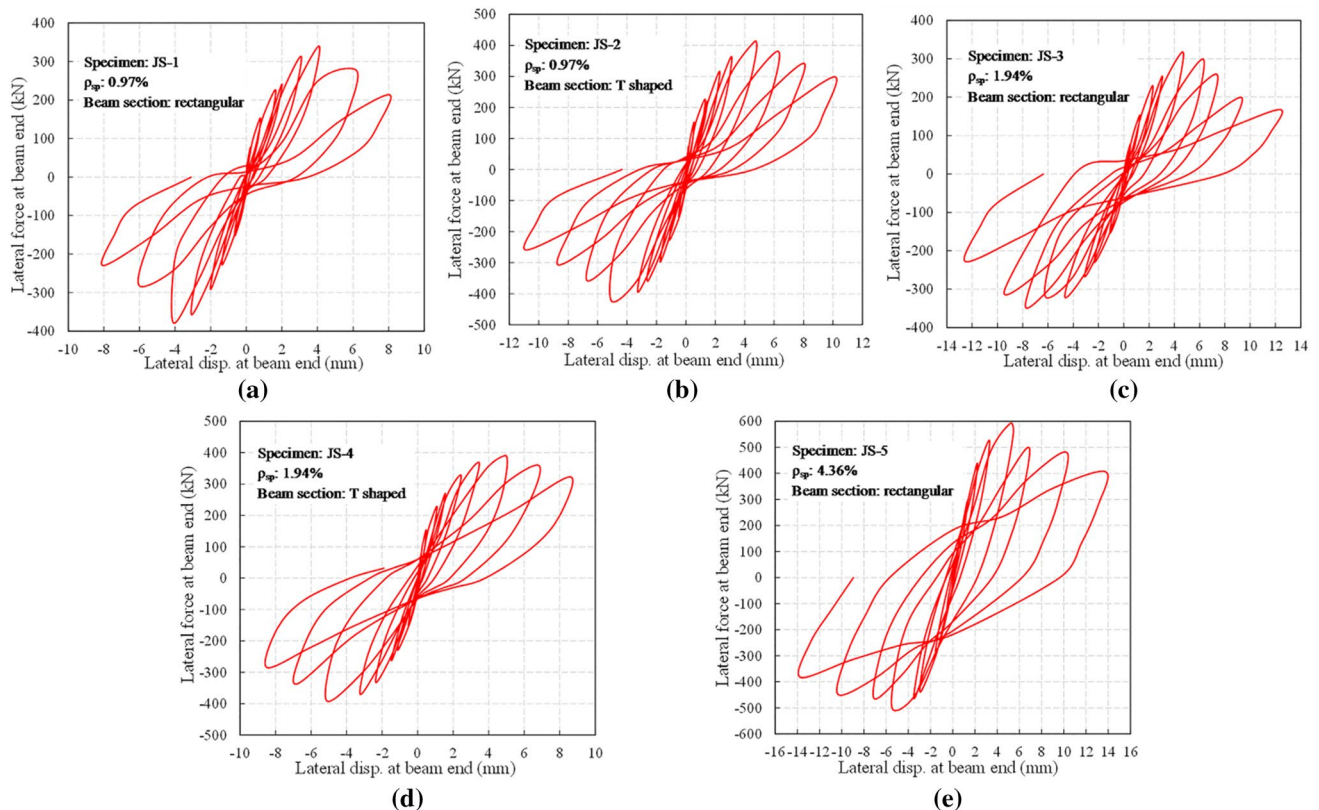
Fig. 6 Measured cyclic shear-displacement relations of specimens: **a** JS-1; **b** JS-2; **c** JS-3; **d** JS-4; **e** JS-5

respectively. For specimens JS-1 and JS-2, where slab was not considered, the corresponding ratios turned out to be 1.43 and 1.38, respectively. For specimen JS-5, since the steel plate contributed most of the shear capacity of the SRC beam, the variation caused by the shear capacity calculation of concrete encasement was the least, the ratio of measured to nominal maximum shear capacity was 1.1.

To estimate the displacement ductility of each specimen, the equivalent energy method was adopted to determine the yield displacement based on the skeleton curve of each specimen. As shown in Fig. 8, V_m is the maximum shear force and corresponding displacement on the skeleton curve; the ultimate condition is defined as the point on the skeleton curve where the shear force is equal to $0.85V_m$ and the corresponding displacement Δ_u is regarded as the maximum displacement. An idealized bilinear curve consisting of an ascending segment and a flat segment corresponding to the maximum shear force V_m is developed in the way illustrated in Fig. 8. If shaded regions (1) and (2), enclosed by the measured skeleton curve and the ascending segment of idealized bilinear curve, have the same area, the displacement corresponding to the intersecting point between the ascending and flat segments of the idealized bilinear curve is taken as the yield displacement. Then the displacement ductility coefficient μ_Δ is the ratio of Δ_u to Δ_y. Table 3 summarizes the displacement ductility coefficient of each specimen. It is obvious that increasing the steel plate ratio can improve the ductility for specimens. With the same steel plate ratio, the existence of slab can also improve the ductility of specimens.

2.4 Stiffness Degradation

The variation of peak-to-peak stiffness against lateral displacement is plotted in Fig. 9. The initial stiffness of specimens JS-2 and JS-4 were much higher than JS-1 and JS-3, showing the influence of slab. However, the significance of slab was effectively lost at very small deformation. In
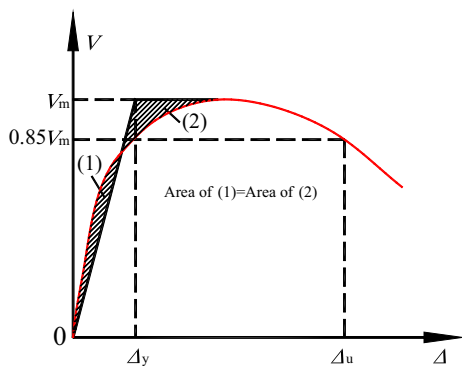
Fig. 8 Energy equivalence method

Table 3 Displacement ductility coefficient

Specimen	Loading direction	Δ_y/mm	Δ_u/mm	μ_Δ	$\bar{\mu}_\Delta$
JS-1	(+)	1.76	5.79	3.29	3.11
	(−)	1.78	5.21	2.93	
JS-2	(+)	1.72	7.64	4.44	4.01
	(−)	1.86	6.65	3.58	
JS-3	(+)	2.32	7.11	3.06	3.61
	(−)	1.96	8.13	4.15	
JS-4	(+)	1.68	8.22	4.89	4.48
	(−)	1.70	6.93	4.08	
JS-5	(+)	2.35	10.78	4.59	4.83
	(−)	2.25	11.41	5.07	

addition, the stiffness degradation characteristics in the positive and negative directions became very similar after the influence of slab was insignificant. The specimen JS-5 exhibited the most gradual stiffness degradation process among all the specimens.

2.5 Finite Element Analysis

The test specimens were numerically simulated using proved reliable finite element analysis program DIANA. The simulated results were then compared with the experimental ones to verify the accuracy of the proposed numerical techniques.

2.6 Modeling of Concrete

Three-dimensional solid elements were used to discretize the wall concrete. The total strain rotating crack model was adopted to simulate the cracking characteristics of concrete. According to this model, when the principle tensile stress exceeds the specified limit, cracks appear in the perpendicular direction. Compared with the fixed crack model, where the direction of cracks are fixed after cracks initiate, the direction of the cracks in the rotating crack model are always perpendicular to the direction of principle tensile stress. The compressive stress–strain relationship of concrete used in the analysis is illustrated in Fig. 10. The parabolic compressive stress–strain relationship of concrete is defined by:

$$\sigma = \begin{cases} -f_c \dfrac{\varepsilon_j}{3\varepsilon_{c/3}} & \varepsilon_{c/3} < \varepsilon_j \leqslant 0 \\ -f_c \dfrac{1}{3}\left(1 + 4\left(\dfrac{\varepsilon_j - \varepsilon_{c/3}}{\varepsilon_c - \varepsilon_{c/3}}\right) - 2\left(\dfrac{\varepsilon_j - \varepsilon_{c/3}}{\varepsilon_c - \varepsilon_{c/3}}\right)^2\right) & \varepsilon_c < \varepsilon_j \leqslant \varepsilon_{c/3} \\ -f_c\left(1 - \left(\dfrac{\varepsilon_j - \varepsilon_c}{\varepsilon_u - \varepsilon_c}\right)^2\right) & \varepsilon_u < \varepsilon_j \leqslant \varepsilon_c \end{cases} \quad (1)$$

where f_c is the compressive strength of concrete; $\varepsilon_{c/3}$, ε_c and ε_u are the concrete strains corresponding to $1/3\ f_c$, f_c
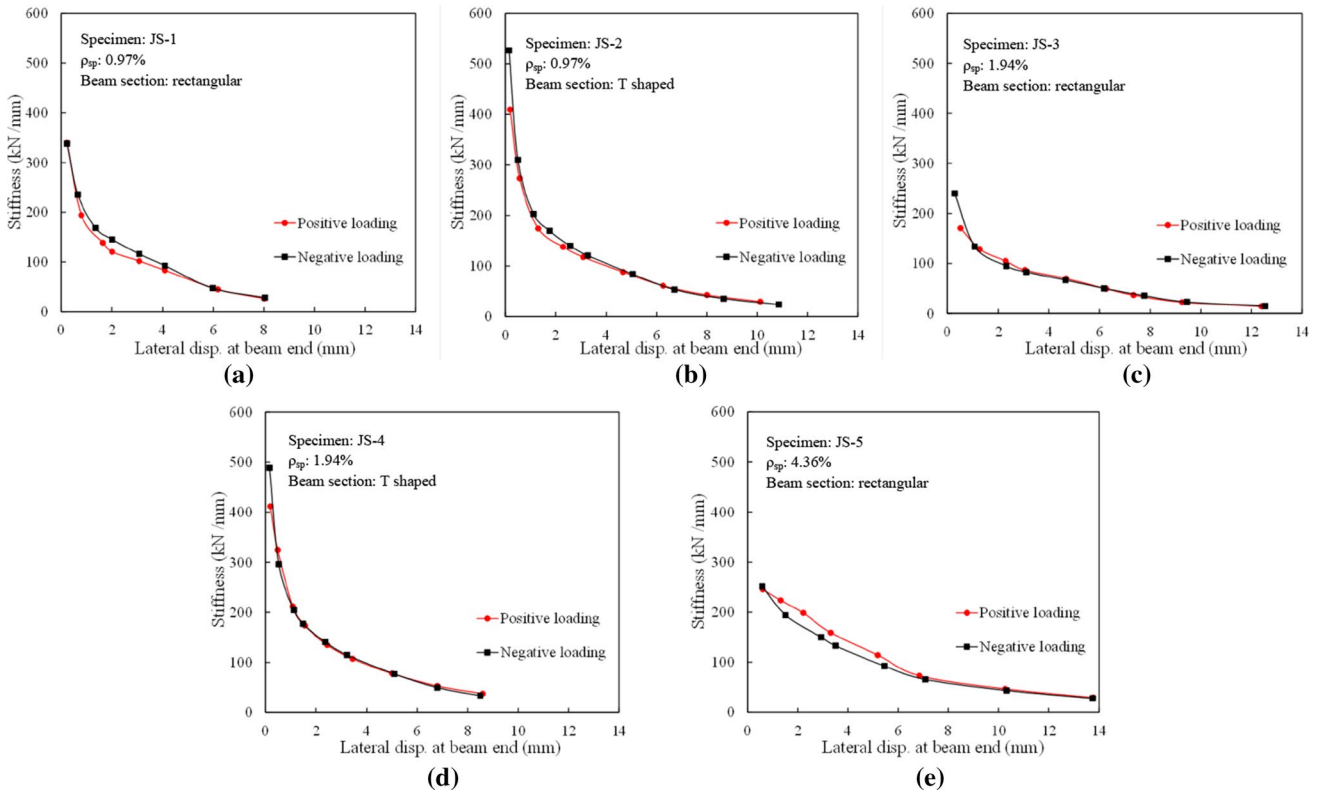
Fig. 9 Stiffness degradation: **a** JS-1; **b** JS-2; **c** JS-3; **d** JS-4; **e** JS-5
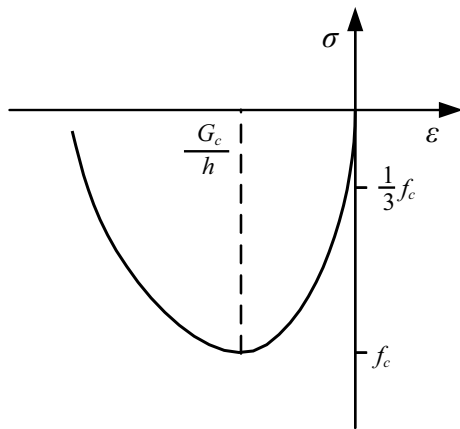
Fig. 10 Compressive stress–strain curve of concrete

and ultimate condition, and can be expressed by Eqs. (2–4) respectively:

$$\varepsilon_{c/3} = -\frac{f_c}{3E}, \tag{2}$$

$$\varepsilon_c = -\frac{5f_c}{3E} = 5\varepsilon_{c/3}, \tag{3}$$

$$\varepsilon_u = \varepsilon_c - \frac{3G_c}{2hf_c}, \tag{4}$$

where E is the Young's modulus; G_C is the total compressive fracture energy of concrete ranging from 10 to 25 N-mm/mm^2.

The tensile stress–strain relationship of concrete used in the analysis is depicted in Fig. 11. The tensile strength of concrete f_t was determined in accordance with GB50010-2010 [21]. ε_0 and ε_u are the tensile strains corresponding to f_t and the ultimate condition, which were taken as 0.000118 and 0.0014, respectively.

2.7 Modeling of Reinforcement and Steel

The modeling of reinforcing bars and embedded steel members was treated differently to balance the simulation accuracy and computational cost. The reinforcing bars were considered using embedded reinforcement model, where the reinforcement element is embedded in the concrete element so that the strain of the reinforcement is compatible with that of concrete element, assuming that the reinforcement is adequately bonded to concrete without slip effect. The flat shell element, on the other hand, was used to model the embedded truss chord and web braces with the consideration
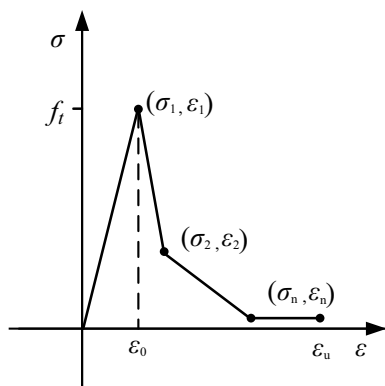
Fig. 11 Tensile stress–strain curve of concrete

of bond-slip law. The tri-linear stress–strain model, as shown in Fig. 12, was used for simulating the reinforcement bars and the shaped steel.

2.8 Bond Slip Consideration

The bond-slip law used in the numerical simulation is depicted in Fig. 13, which is based on CEB-FIP model code. The set of equations of bond stress for different segments of the curve are described as follows:

$$\tau = \tau_{\max}\left(\frac{s}{s_1}\right)^{\beta} \quad 0 \leqslant s \leqslant s_1, \tag{5}$$

$$\tau = \tau_{\max} \quad s_1 \leqslant s \leqslant s_2, \tag{6}$$

$$\tau = \tau_{\max} - \left(\tau_{\max} - \tau_{\mathrm{f}}\right)\frac{s - s_1}{s - s_2} \quad s_2 \leqslant s \leqslant s_3, \tag{7}$$

$$\tau = \tau_{\mathrm{f}} \quad s_3 \leqslant s, \tag{8}$$

where τ is the bond stress; $\tau_{\max}$ is the bond strength; τ_{f} is the residual bond stress; s is the relative slip between steel and concrete; s_1, s_2 and s_3 are characteristic slip values; β is an empirical coefficient. The parameters in the bond stress law depended on the steel surface condition.
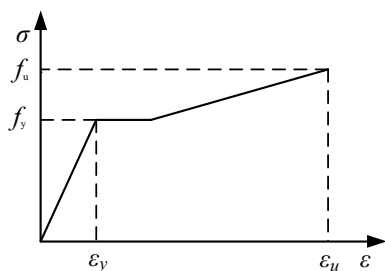
Fig. 12 Stress–strain relationship of steel
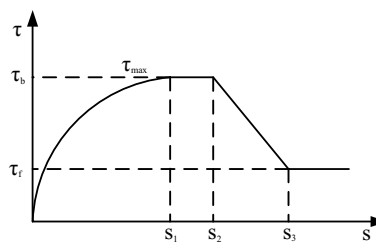
Fig. 13 Bond-slip law

2.9 Meshing of Finite Element Models of Test Specimens

The meshing of the finite element models is important to the analysis. Although a more refined meshing can generally result in analysis results with better accuracy, the computational cost will be largely increased or even cause difficulty in convergence. In the present study, the clear height and width of shear walls were equally divided into 20 and 10 segments with 60 and 90 mm segment lengths, respectively. The coupling beam with the 450 mm height and 300 mm width were equally divided into 15 and 10 segments, respectively. And the thickness of shear wall and coupling beam were equally divided into 4 segments with 55 mm segment length. Although the element size can be further reduced to obtain a more refined meshing scheme, no obvious difference in calculation results was observed.

2.10 Solution Algorithm

The Regular Newton–Raphson method was adopted for the solution algorithm of the nonlinear functions. Compared with the Modified Newton–Raphson method, more precise results can be calculated by the regular Newton–Raphson method. The energy convergence standard was adopted to determine if the iteration was converged or not. The convergence toleration was 0.001 after the maximum iteration number of 30 times.

3 Comparison of Simulated and Experimental Results

The numerical simulation was carried out to evaluate the overall load–deformation behavior of specimens. The resulted load–deformation skeleton curves and hysteresis loops were compared with the corresponding experimental results to verify the effectiveness and accuracy of the proposed numerical techniques for the analysis of load carrying

capacity, initial stiffness, ductility, behavior and response characteristics of specimens.

Figures 14, 15, 16, 17 and 18 show the comparison results of the skeleton and hysteretic load–displacement relations obtained from the experiments and analysis. It is noted that the load–displacement relations depicted herein reflect the mechanical behavior of SRC beams and their connection to wall piers. Considering the fact that the endplate joint between steel beam and steel column was completely embedded in the boundary region of wall pier, the modeling of the endplate connection was simplified to be rigid. This assumption was reasonable at the entire loading process, which can be proved by the rather good agreement between the experimental and analytical skeleton curves in terms of initial stiffness, maximum load carrying capacity and post-yield response. The loading, unloading and reloading

Fig. 14 Comparison of analytical and experimental results of JS-1: **a** skeleton curve; **b** hysteretic loops
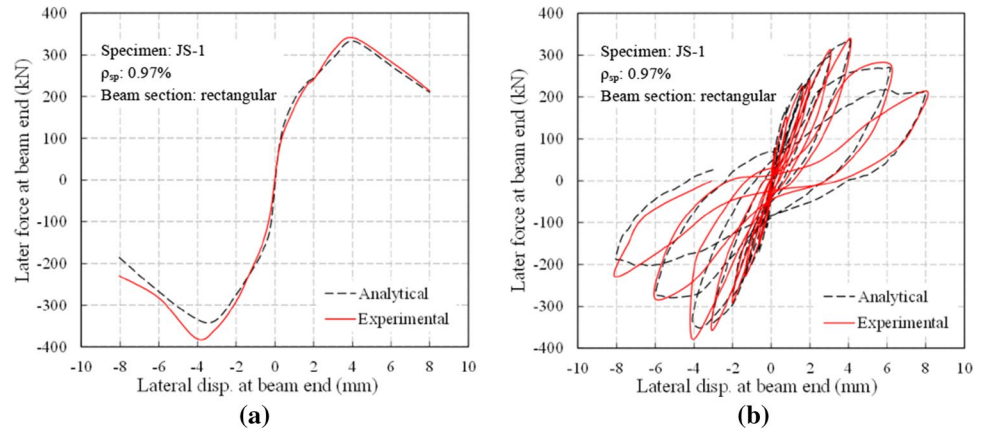
Fig. 15 Comparison of analytical and experimental results of JS-2: **a** skeleton curve; **b** hysteretic loops
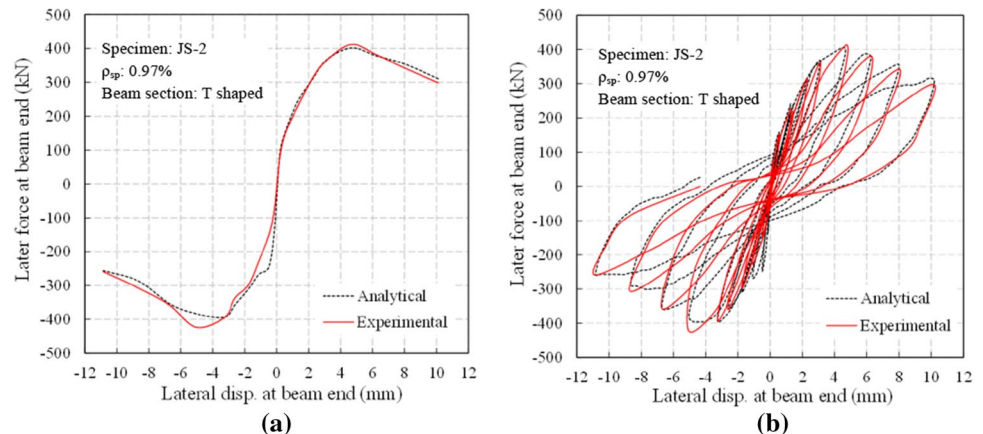
Fig. 16 Comparison of analytical and experimental results of JS-3: **a** skeleton curve; **b** hysteretic loops
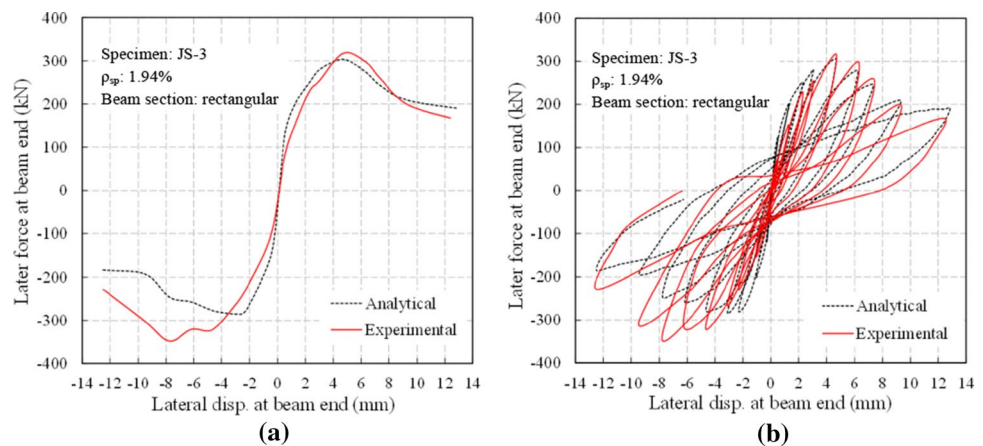
Fig. 17 Comparison of analytical and experimental results of JS-4: (a) Skeleton curve; (b) Hysteretic loops
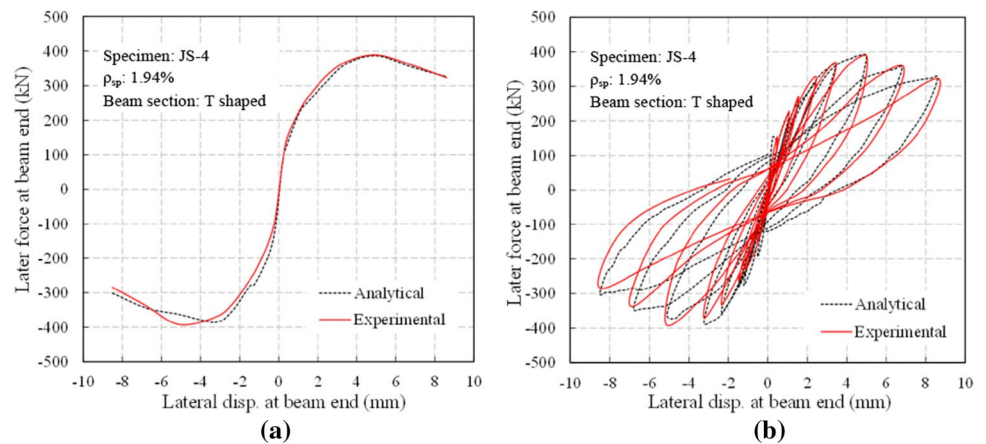
Fig. 18 Comparison of analytical and experimental results of JS-5: **a** skeleton curve; **b** hysteretic loops
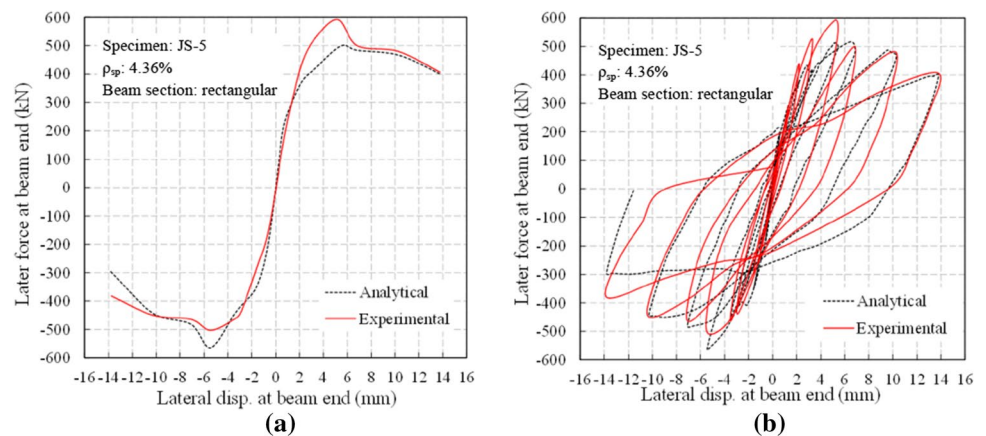
branches of the experimental and analytical hysteretic loops agreed satisfactorily well in the overall sense. However, the analytical results of specimens JS-1 to JS-4 did not reflect very well the pinching effect observed in experimental loops, especially for the last loading cycles, which is because the numerical models cannot reflect that for last loading cycles the concrete of beam crushed so severely that the internal force transfer mechanism between concrete encasement and embedded steel plate was significantly weakened.

4 Conclusions

The seismic performance of bolted endplate connections between steel and concrete SRC coupling beams to SRC shear walls was examined by experimental investigation and finite element numerical simulation. Based on the experimental observations and results from numerical studies, the following conclusions can be drawn:

1. The existence of slab can improve the strength, initial stiffness and ductility of SRC beam-wall subassembly with bolted endplate connection. No matter the slab influence is considered or not in design, the resulted SRC beams shall possess higher strength than expected in design. It is reasonable to design the beam-wall joint based on 1.6 times the nominal beam capacity.

2. Increasing the steel plate ratio for SRC coupling beam can effectively enhance the strength, stiffness and ductility. In addition, the energy dissipation capacity of the SRC beam can be significantly improved using a steel plate ratio of 5%.

3. The bolted endplate connection can be designed to satisfactorily ensure the SRC coupling beams to develop their strength, deformation and energy dissipation capacities. Although cracks will be developed in the early loading stage, the post-yield inelastic damages will be concentrated to the SRC beam.

4. The hysteretic curves and skeleton curves simulated by the finite element analysis agreed well with those obtained in experiments, showing the effectiveness and accuracy of the suggested numerical techniques.

References

1. Zhao QH, Astaneh-Asl A (2004) Cyclic behavior of traditional and innovative composite shear walls. J Struct Eng 130(2):271–284
2. Dan D, Fabian A, Stoian V (2011) Theoretical and experimental study on composite steel–concrete shear wall with vertical steel encased profiles. J Constr Steel Res 67(5):800–813
3. Dan D, Fabian A, Stoian V (2011) Nonlinear behavior of composite shear walls with vertical steel encased profiles. Eng Struct 33(10):2794–2804
4. Hu HS, Nie JG, Fan JS, Tao MX, Wang YH, Li SY (2016) Seismic behavior of CFST-enhanced steel plate-reinforced concrete shear walls. J Constr Steel Res 119:176–189
5. Lam WY, Su RKL, Pam HJ (2005) Experimental study on embedded steel plate composite coupling beams. J Struct Eng 131(8):1294–1302
6. Gong BN, Shahrooz BM (2001) Concrete-steel composite coupling beams. I: component testing. J Struct Eng 127(6):625–631
7. Gong BN, Shahrooz BM (2001) Concrete-steel composite coupling beams. II: subassembly testing and design verification. J Struct Eng 127(6):632–638
8. Nie JG, Hu HS, Eatherton MR (2014) Concrete filled steel plate composite coupling beams: Experimental study. J Constr Steel Res 94:49–63
9. Kulkarni SA, Li B, Yip WK (2008) Finite element analysis of precast hybrid-steel concrete connections under cyclic loading. J Constr Steel Res 64(2):190–201
10. Wu YT, Xiao Y (2009) Seismic behavior of PC column and steel beam composite moment frame with post-tensioned connection. J Struct Eng ASCE 135(11):1398–1407
11. Prinz GS, Nussbaumer A, Borges L, Khadka S (2014) Experimental testing and simulation of bolted beam-column connections having thick extended endplates and multiple bolts per row. Eng Struct 59:434–447
12. Mohamadi-Shooreh MR, Mofid M, McCabe SL (2012) Empirical model of the moment-rotation curve of beam-to-beam bolted flush endplate connections. J Struct Eng ASCE 139(1):66–72
13. Asghari A, Zarnagh BA (2017) A new study of seismic behavior of perforated coupled shear walls. Int J Civ Eng 15(5A):775–789. https://doi.org/10.1007/s40999-017-0174-y
14. Choi HK (2017) Experimental study on shear wall with slab and openings. Int J Civ Eng 15(4A):451–471. https://doi.org/10.1007/s40999-016-0078-2
15. Hung CC, Lu WT (2017) Tall hybrid coupled structural walls: seismic behavior and design suggestions. Int J Civ Eng. https://doi.org/10.1007/s40999-017-0162-2
16. Qun X, Song X, Lei X (2017) Study on seismic damage model of post-installed connection between steel and concrete. Int J Civ Eng. https://doi.org/10.1007/s40999-017-0277-5
17. Wang QW, Shi QX, Tian HH (2016) Experimental study on shear capacity of SRC joints with different arrangement and sizes of cross-shaped steel in column. Steel Compos Struct 21(2):267–287
18. GB50011-2010 (2010) Code for seismic design of buildings. China Architecture & Building Press, Beijing **(in Chinese)**
19. JGJ138-2016 (2016) Code for design of composite structures. China Architecture & Building Press, Beijing **(in Chinese)**
20. Li X, Wu YT, Mao WF, Xiao Y, Anderson JC, Guo YR (2006) Bolted end plate connections for steel reinforced concrete composite structures. Struct Eng Mech 24(3):291–306
21. GB50010-2010 (2010) Code for design of concrete structures. China Architecture & Building Press, Beijing **(in Chinese)**